Catalysis Today 289 (2017) 20–28

Contents lists available at ScienceDirect

Catalysis Today

journal homepage: www.elsevier.com/locate/cattod

The multiple benefits of glycerol conversion to acrolein and acrylic acid catalyzed by vanadium oxides supported on micro-mesoporous MFI zeolites

Luiz G. Possato, Thiago F. Chaves, Wellington H. Cassinelli, Sandra H. Pulcinelli, Celso V. Santilli, Leandro Martins*

Instituto de Química, UNESP – Univ. Estadual Paulista, Rua Prof. Francisco Degni 55, 14800-060, Araraquara, SP, Brazil

ARTICLE INFO

Article history:
Received 12 April 2016
Received in revised form 20 July 2016
Accepted 2 August 2016
Available online 16 August 2016

Keywords:
Glycerol oxidehydration
V_2O_5/MFI catalyst
Acrolein
Acrylic acid
Micro-mesoporous zeolites

ABSTRACT

The ZSM-5 zeolite (MFI structure, Si/Al = 40) was treated using NaOH and either oxalic acid or HCl to obtain hierarchical materials with different characteristics, followed by impregnation with vanadium oxides (V_2O_5) to generate redox-active sites. The impact of the multiple treatments on the efficiency and stability of the catalysts in the conversion of glycerol to acrolein and acrylic acid was investigated and correlated with catalyst porosity, acidity, and chemical composition. The treated and impregnated V_2O_5 catalysts were subjected to XRD, ^{27}Al NMR, nitrogen physisorption, TPD-NH_3, TG, and UV–Vis analyses, in order to associate the properties of the catalysts with their activities. The studies showed that the catalytic performance of the materials depended on the acidic and textural properties of the zeolites, which influenced both the dispersion of V_2O_5 and its interaction with the acid sites of the supporting zeolites. All the catalysts provided conversion values exceeding 65%, even after 6 h on glycerol stream. The distribution of products strongly reflected the effects of pore formation, acid treatment with oxalic acid or HCl, and the presence of vanadium oxide. The effects of these modifications resulted in higher selectivity to acrolein and acrylic acid, a reduced rate of coke accumulation in the zeolite, and a longer catalyst lifetime.

1. Introduction

The growth of greenhouse gas emissions and the limited reserves of easily extracted fossil fuels have led researchers and industry to pursue new alternatives to replace, even partially, the use of fossil fuels. As a result, the use of compounds derived from biomass, such as biogas, ethanol from sugarcane, and biodiesel has increased in recent years. In the case of biodiesel, production has increased and consequently there has been an increase in the concomitant formation of coproduced glycerol [1–3].

Glycerol is a focus of green catalytic processes, because this molecule offers interesting chemical versatility that can be exploited for the formation of compounds that are currently provided by the petrochemical industry. An example of glycerol valorization is the synthesis of 1,2-propanediol and 1,3-propanediol, which are used as antifreeze fluids in automobiles. In industry, both compounds are obtained from the hydration of propene. However, a high conversion and selectivity to glycols has been obtained by glycerol hydrogenolysis using catalysts based on metallic Ni, Ru, and Cu [4–7].

Another important conversion of glycerol into petrochemical-type compounds is the formation of acrolein and acrylic acid, which are used in the manufacture of resins. Acrolein can be obtained by gas phase glycerol dehydration on acid catalysts such as heteropolyacids [8], impregnated phosphate groups on metal oxides [9], sulfated zirconia [10], Nb_2O_5 [11], mixed oxides [12], zeolites [13–15], functionalized mesoporous silica [16,17], and vanadium-silicates [18]. The glycerol can also be dehydrated in liquid phase [19,20]. Acrylic acid is obtained from the oxidation of acrolein. The one-step conversion of glycerol into acrylic acid using bifunctional catalysts with acid and redox sites occurs according to Scheme 1 [21–26]. An interesting aspect of coupling the two reactions is the mutually supporting endothermic dehydration of glycerol ($\Delta H^0 = 3.04$ kcal/mol) and exothermic oxidation of acrolein ($\Delta H^0 = -61.02$ kcal/mol).

For glycerol dehydration using zeolites, maximum performance of the catalyst is achieved by combining Brønsted acid sites of medium strength (strong acid sites lead to severe coke formation,

* Corresponding author.
E-mail address: leandro@iq.unesp.br (L. Martins).

http://dx.doi.org/10.1016/j.cattod.2016.08.005
0920-5861/

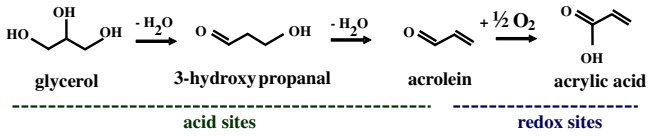

Scheme 1. Glycerol oxidehydration (dehydration combined with oxidation) on bifunctional acid and redox active sites.

while weak acid sites are less capable of converting glycerol) [27], porosity (which enhances the diffusion of glycerol and acrolein), and high specific area (which increases access to catalytic sites). For instance, members of the lamellar MWW zeolite family, which includes microporous MCM-22, pillared MCM-36, and delaminated ITQ-2, offer advantageous characteristics for glycerol dehydration [22]. Following pillarization and delamination of the MWW structure, the strengths of acid sites decrease, but the increases in mesopores and specific area raise the overall performance of the catalyst [28].

Despite the attraction of lamellar zeolites for use in glycerol dehydration, the laborious multiple steps and the expense associated with catalyst preparation are notable disadvantages. Alternatively, the desilication of commercially available zeolites by treatment with sodium hydroxide solution seems to be more practical [29,30]. The alkaline process is simple, with hydroxyl groups attacking and removing silicon atoms from the zeolite structure, creating randomly distributed pores in the zeolite crystals. The diameter and volume of the pores can be tuned by adjusting the concentration of the alkaline solution and by varying the exposure time of the zeolite (usually a few minutes) and the desilication temperature (which normally ranges from room temperature to a few tens of degrees Celsius) [31–37]. The broad distribution of mesopore families results in catalytic performance in glycerol dehydration similar to that of the MWW zeolites.

A disadvantage of the desilication method is that during the zeolite treatment process, aluminum atoms are removed as well as silicon atoms. Silicon species are mostly found in the alkaline liquid phase, but aluminum tends to form insoluble oligomeric species that can precipitate on the catalyst surface as extra-framework aluminum atoms (EFA). Consequently, the mesopores created are obstructed due to an alkali-induced alumination of the external surfaces of the crystals, and the nature of the acid sites of the zeolite shifts from Brønsted to Lewis acid sites. This catalytic acid behavior must be considered in the design of catalysts by desilication, because EFA sites are selective in converting glycerol into undesirable byproducts. However, the EFA can be removed from the zeolite by acid leaching; as a result, the selectivity to acrolein is enhanced and the diffusion of chemicals through the pores is increased due to the removal of aluminum species.

In the second step of glycerol conversion to acrylic acid (Scheme 1), redox active sites are required. Vanadium oxides are strong candidates for this purpose because they possess a very important redox characteristic, namely the capacity to adopt multiple oxidation states. On these catalysts, acrolein is oxidized by removing a surface oxygen atom from V_2O_5, giving rise to acrylic acid and an oxygen vacancy in V_2O_{5-x}. In a subsequent step, the catalytic site is oxidized and reestablished by feeding an excess of molecular O_2 in the stream ($V_2O_{5-x} + {}^1/_2O_2 \rightarrow V_2O_5$). This redox mechanism and the changes in V^{5+}/V^{4+} oxidation states during the catalytic reaction are known as the Mars-Van Krevelen mechanism [38].

In a recent publication, we described additional useful features of the V_2O_5/zeolite catalytic system [20]. Besides the advantages mentioned above, vanadium oxides supported on zeolites were much less susceptible to deactivation, compared to the bare zeolites. Several parallel and unknown reactions occur simultaneously with glycerol dehydration to acrolein. Byproducts include acetaldehyde, acetol, and acetic acid, as well as very harmful and deactivating coke molecules. After catalytic experiments with bare zeolites, the polymerization of bulky molecules on the surfaces of the catalysts led to coke formation and a characteristic black appearance. However, in the previous work it was found that when a V_2O_5/zeolite catalyst was used, the coke was continuously oxidized due to the presence of well-dispersed vanadium oxides on the zeolite surface, which maintained the catalytic sites active for longer periods.

The aim of the present work was to explore further the multiple benefits of porous V_2O_5/MFI catalysts in the one-step glycerol conversion to acrylic acid. The work focused on zeolite supports prepared by sequential processes of desilication (in NaOH solution) and dealumination (in HCl or oxalic acid solutions) in order to tailor the pores and the quality of acid sites derived from either aluminum in tetrahedral coordination in the zeolite or from EFA. Improved transformation of glycerol was achieved on the micro-mesoporous V_2O_5/MFI zeolites, due to higher catalytic conversion, improved selectivity to acrolein and acrylic acid, extended catalyst stability, and decreased coke formation.

2. Experimental

2.1. Preparation of zeolite supports

Zeolite of MFI structure (Si/Al mole ratio of 40) was kindly provided by Zeolyst (USA). The sample was submitted to alkaline treatment at 60 °C for 1 h using an aqueous solution of NaOH (0.6 mol/L). Detailed information concerning the desilication procedure is provided elsewhere [30,39]. The desilicated zeolite was then submitted to two different acid treatments using aqueous solutions of hydrochloric or oxalic acids. The acidic treatments were performed under reflux using 0.1 mol/L acid solution. The MFI supports were denoted A (parent and untreated MFI zeolite), B (after alkaline treatment), C (after treatment using $H_2C_2O_4$), and D (after treatment using HCl). After the sequential alkaline and acidic treatments, all the supports (A, B, C, and D) were ion exchanged three times with NH_4NO_3 solution, at room temperature. The exchanged NH_4^+ cations were thermally decomposed by heating the samples for 3 h in a conventional muffle furnace, in air atmosphere, from 25 °C to 500 °C at a heating rate of 10 °C/min.

2.2. Preparation of the catalysts

V-MFI catalysts were obtained by incipient wetness impregnation of the supports using an aqueous solution of vanadyl sulfate (0.05 mol/L). Approximately 50 mL slurry of vanadyl sulfate solution and zeolite was stirred for 1 h at 25 °C. The water was allowed to evaporate under vacuum at 40 °C, and the samples were dried overnight at 100 °C. Finally, the catalysts were subjected to a thermal treatment for 2 h in an air atmosphere, with heating from 25 °C to 500 °C at a rate of 5 °C/min. The contents of V_2O_5 in all the samples was 10 wt.%.

2.3. Characterization of samples

X-ray diffractograms of the supports and catalysts were obtained at the XPD beamline of the Brazilian Synchrotron Light Laboratory (LNLS), using a Huber 4+2 circle diffractometer equipped with an Eulerian cradle (model 513) placed approximately 13 m from the double-bounce Si(111) monochromator ($\lambda = 1.377494$ Å) [40]. The data were collected in high-resolution mode, employing a Si(111) analyzer crystal and a Mythen detector. Structural parameters were determined by the Rietveld profile method, using GSAS-EXPGUI software [41,42]. The scale factors,

zero shifts, and backgrounds of the peak profiles, together with the lattice parameters, were refined by fitting with a sixth order Chebyshev polynomial. Pseudo-Voigt functions were employed for the peak profile refinements. Other parameters were not refined.

The textural properties of the supports and impregnated catalysts were determined by means of nitrogen adsorption-desorption isotherms obtained at −196 °C with a Micromeritics ASAP 2010 instrument, using a relative pressure (P/P_0) interval of 0.001-0.998. The samples were previously decontaminated by degassing for 12 h at 100 °C under a vacuum of 1×10^{-5} Pa. The t-plot method was used to distinguish between the micro- and mesopore contributions. Finally, the mesopore distribution was estimated using the BJH method [24].

The ^{27}Al NMR spectra were acquired using a Varian INOVA 500 spectrometer equipped with a 7 mm probe and operated at 4.5 kHz. The experiments were performed using a spinning rate of 78.2 MHz, acquisition time of 15.4 ms, pulse width of 2.4 μs, and recycle delay of 0.1 s. The ^{27}Al chemical shifts were referenced to an aqueous solution of $Al(NO_3)_3$ (1 mol/L). Each spectrum was the result of 256 scans.

Thermogravimetric analyses of the used catalysts (after the glycerol reaction) were performed with a TA Instruments SDT Q600 thermobalance. The samples were heated from 30 to 900 °C, at 10 °C/min, under a 100 mL/min flow of synthetic air.

Scanning electron microscopy (SEM) analyses of the samples were performed using an Inspect S50 microscope (FEI) operated at 10 kV, with a secondary electron detector and working distance of 10 mm. After 1 h in an ultrasonic bath, a suspension consisting of the sample and acetone was deposited on an aluminum stub specimen mount. The Si/Al mole ratio was determined by energy dispersive X-ray spectroscopy (EDS), using the same microscope. The spectra were measured in five different regions, and the composition was determined by averaging the results obtained for each sample.

The acid sites of the calcined catalysts were determined by temperature programmed desorption of ammonia (TPD-NH_3). Previously, a 200 mg portion of each sample was degassed at 300 °C for 1 h under a 60 mL/min flow of helium. The temperature was then decreased to 100 °C and the sample was exposed for 1 h to a flow of 1% ammonia in helium (60 mL/min). After surface saturation, the sample was submitted to helium treatment at 100 °C for 1 h to remove physisorbed ammonia. The TPD-NH_3 analysis was performed from 100 °C to 600 °C (at 10 °C/min), under a 60 mL/min flow of helium. The desorbed ammonia was monitored and quantified with a Pfeiffer vacuum mass spectrometer connected to the outlet stream of the tubular reactor.

2.4. Catalytic tests

The bare zeolite and V-MFI catalysts were tested for glycerol dehydration and oxidehydration, respectively, at atmospheric pressure. Previously, 100 mg portions of the samples were heated at 300 °C for 15 min, under a 30 mL/min flow of nitrogen. The glycerol dehydration reaction was performed in a fixed-bed reactor at 300 °C for 6 h, using a solution of 10 wt.% glycerol in water. A flow of 0.05 mL/min of this liquid solution was introduced to a heated line using a syringe pump (KD Scientific), and the glycerol was transported to the reactor using a 30 mL/min flow of nitrogen. The unconverted glycerol and the reaction products were condensed continuously in a gas-liquid separator kept at 1 °C. The liquid was periodically collected, weighed, and injected into a gas chromatograph (Model GC-2014, Shimadzu) equipped with a capillary column (Rtx-1, 30 m, 0.32 mm, 1 μm) and a FID detector. For each injection, a known mass of *n*-butanol was used as internal standard. Four drops of standardized solution was diluted in isopropanol (1 mL) to prevent excess water from the chromatographic column. The GC analyses were performed in triplicate, and the retention times of all the compounds were compared with those of authentic standards. The glycerol conversions ($X_{glycerol}$) and product selectivities (S) were calculated using the following equations:

$$X_{glycerol}(\%) = \frac{n_{Gl}{}^{input} - n_{Gl}{}^{output}}{n_{Gl}{}^{input}} \times 100 \quad S(\%) = \frac{n_i}{n_{Gl}{}^{input} - n_{Gl}{}^{output}} \times \frac{Zi}{Z_{Gl}} \times 100$$

where:

$n_{Gl}{}^{input}$ and $n_{Gl}{}^{output}$ are the input and output flows of glycerol;

n_i is the flow of the products *i* (mol/min);

$Z_{Gl} = 3$ (the number of carbon atoms in the glycerol molecule);

Z_i = number of carbon atoms in the products.

The deactivation (*D*) of the catalysts used in the glycerol dehydration was calculated using:

$$D(\%) = \frac{(X_{glycerol})_{at\ time\ zero} - (X_{glycerol})_{after\ 6h}}{(X_{glycerol})_{at\ time\ zero}} \times 100$$

The glycerol oxidehydration reaction was conducted following the same protocol as glycerol dehydration, but with the reaction temperature shifted to 350 °C and with 20% of oxygen fed into the stream (6 mL/min of O_2 and 24 mL/min of N_2). The O_2/glycerol mole ratio of 4.5 ensured that an excess of oxygen was used.

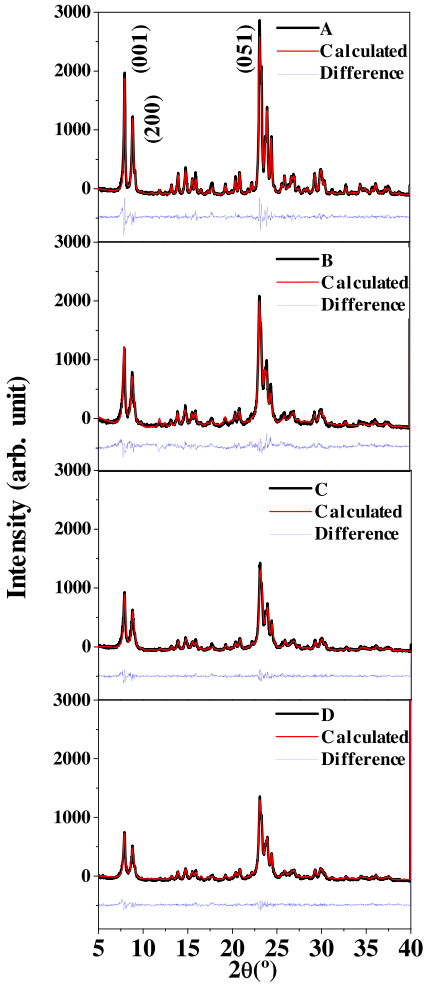

Fig. 1. Rietveld plots of samples A (parent MFI), B (NaOH), C ($H_2C_2O_4$), and D (HCl), using λ = 1.3775 Å: experimental (black line), calculated (red line), and difference plot (blue line). (For interpretation of the references to colour in this figure legend, the reader is referred to the web version of this article.)

3. Results and discussion

3.1. Characterization of the zeolite supports

The XRD patterns of the MFI zeolites before treatment (sample A in Fig. 1), after the alkaline treatment (sample B), and after the acidic treatments (samples C and D) revealed the presence of the main reflections related to the MFI structure: (011), (200), and (051). The samples submitted to the treatments showed decreases in peak intensity, consistent with the reduction of long-range order caused by the extraction of silicon and aluminum atoms from the MFI structure [35]. The oxalic acid and HCl treatments also affected the crystallinity of the samples, as clearly shown in the diffraction patterns of catalysts C and D, respectively.

The results of structural analysis by Rietveld refinement indicated unit cell expansion after the alkaline treatment [43] (Table 1). The removal of silicon (which has a mean Si-O bond length of 0.162 nm) and the consequent increase in the concentration of aluminum in the structure (mean Al-O bond length of 0.175 nm) caused unit cell expansion from 5236.9 nm^3 to 5258.1 nm^3 [44,45]. The unit cell expansion was additionally influenced by the presence of aluminum atoms that remained in oligomeric form inside the pores of the zeolites. The subsequent acid treatments caused partial leaching of the EFA, and the structural analyses of these samples indicated changes in unit cell volume. The decreased unit cell volumes of the acid treated samples (C and D) revealed that the treatments were effective. The global chemical analyses of the supports showed growth in the aluminum fraction from sample A to sample B (Si/Al ratios of 40 and 18, respectively), and growth in the silicon fraction from sample B to samples C and D.

Samples C and D were (Table 1) dissimilar in terms of both unit cell volume and aluminum fraction, due to the differences in the strengths of the acids used (the pKa values of hydrochloric acid and oxalic acid are −6.3 and 1.2, respectively) and the mechanism of EFA leaching. The action of HCl involved solubilization of oligomeric aluminum oxide species, while oxalic acid acted as both an acid and a chelating agent.

The formation and leaching of EFA was followed using ^{27}Al MAS-NMR (Fig. 2). The chemical shift peak centered at 54 ppm was due to tetrahedral aluminum atoms in the zeolite structure, while the signal between 0 and −20 ppm was due to the octahedrally coordinated aluminum of EFA [46]. As mentioned before, the desilication process was not only responsible for the extraction of silicon atoms from the structure, but also for aluminum removal, as is clearly shown in the detail of the decomposed lines for desilicated sample B. In contrast, the parent zeolite contained only a minor amount of EFA. A rigorous comparison of the NMR spectra showed that the peak at 54 ppm became slightly broadened after the chemical processes, because the tetrahedral arrangement of the aluminum atoms in the structure tended to distort. The same effect led to reduced crystallinity of samples B, C, and D.

The relative intensities of the peaks in the NMR spectra were used for approximate calculation of the amounts of EFA (Table 1). Comparison of the results for Si/Al_{global} and the percentage of EFA showed that the oxalic acid treatment provided greater selectivity in removal of EFA without severely affecting the aluminum framework. The micropore volume only changed slightly, from 0.23 to 0.21 cm^3/g, while the mesopore volume showed a more significant change, from 0.41 to 1.25 cm^3/g (Table 1). The reactivity of HCl was evidenced by a more pronounced reduction of the micropore volume to 0.18 cm^3/g. Dealumination of zeolites with oxalic acid occurs because oxalic acid acts as a hydrolyzing agent by both solubilizing and removing aluminum oxohydroxide species, and forming aluminum oxalate complexes [47]. These complexes have a maximum size of around 0.64 nm, which is compatible with the pore dimensions of zeolites and enables mobility of the complexes within the pores [44].

The N_2 adsorption-desorption isotherms of the MFI zeolites are shown in Fig. 3a. Sample A exhibited a Type I isotherm typical of a pure MFI microporous structure [48]. After the alkaline treatment, a hysteresis loop appeared and the capacity of this sample to adsorb N_2 increased, especially at relative pressure (P/P_0) above 0.8, due to the creation of intra-crystalline mesopores. Additionally, the disruption of the micropore structure of the zeolite in alkaline solution led to a decrease of the adsorption plateau at low P/P_0 characteristic of nitrogen adsorption limited by the micropore size. Analyses of the BJH pore size distribution (Fig. 3b) showed the creation of mesoporosity in the supports submitted to alkaline and acidic treatments. The pore size distributions broadened after use of the acid treatments to clean the zeolite surface, giving rise to additional porosity.

The acid sites of the samples were characterized by temperature-programmed desorption, using ammonia as a basic probe molecule. The TPD-NH_3 curves obtained for the bare and impregnated zeolites are shown in Fig. 4. The bare zeolite showed well-resolved NH_3 desorption peaks, one in the low temperature (LT) region at around 200 °C, and one in the high temperature (HT) region at around 420 °C (Fig. 4a). The reference sample (γ-Al_2O_3) presented a low amount of desorbed NH_3 and a wide desorption temperature range, characteristic of the presence of Lewis acid sites. The amounts of NH_3 desorbed from the samples are given in Table 1. The NaOH treatment resulted in increased NH_3 desorption, due to the decrease in the Si/Al ratio (Table 1), in agreement with the results of the ^{27}Al NMR and chemical analyses. Treatment of zeolite sample B with oxalic acid led to a decrease in the quantity of acidic sites, due to the removal of EFA, as found in the ^{27}Al NMR analyses. The treatment with HCl was less effective in removing the EFA, so the acidity was greater than for the sample treated with oxalic acid [49].

Table 1
Chemical and textural properties of the bare and impregnated zeolite samples.

Samples	V_{micro} (cm^3/g)	V_{meso} (cm^3/g)	μmol of NH_3/g	Si/Al_{global}[a]	% EFA[b]	Unit cell volume (nm^3)
A	0.33	0	388	40	12	5236.9
B – NaOH	0.23	0.41	464	18	29	5258.1
C – $H_2C_2O_4$	0.21	1.25	406	24	5	5250.0
D – HCl	0.18	1.30	529	26	11	5236.6
Reference Al_2O_3	0	0.89	110	n/a[c]	n/a	n/a
V-A	0.26	0	579	n/a	n/a	n/a
V-B	0.18	0.21	545	n/a	n/a	n/a
V-C	0.21	0.24	427	n/a	n/a	n/a
V-D	0.20	0.24	581	n/a	n/a	n/a

[a] Silicon to aluminum mole ratio determined by EDX (global chemical composition).
[b] % EFA determined by deconvolution of the ^{27}Al NMR spectrum (contribution of tetrahedral aluminum species in the zeolite framework).
[c] Not applicable.

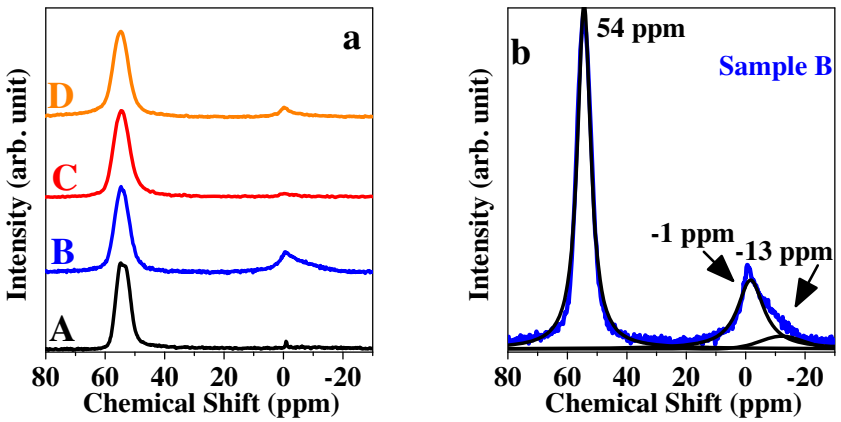

Fig. 2. (a) ^{27}Al NMR spectra of the parent and treated zeolites, and (b) deconvolution of the sample B spectrum.

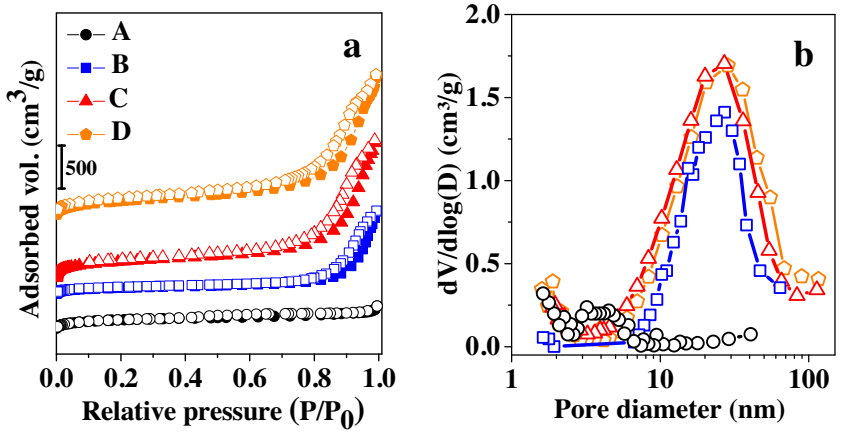

Fig. 3. (a) Nitrogen adsorption-desorption isotherms (filled and empty points correspond to nitrogen adsorption and desorption, respectively), and (b) BJH mesopore size distributions from the desorption branches.

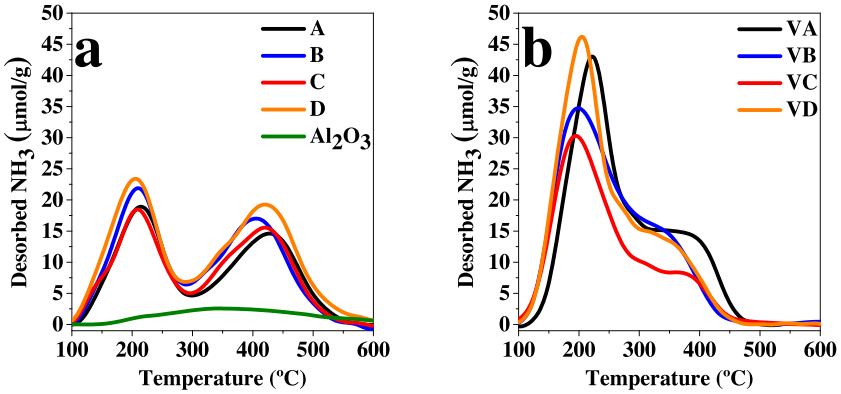

Fig. 4. Temperature-programmed desorption of ammonia (TPD-NH_3) curves for (a) the bare zeolites, and (b) the impregnated zeolites.

The TPD-NH_3 curve profiles of the vanadium oxide-impregnated samples (Fig. 4b) were significantly different, compared to those of the bare zeolites (Fig. 4a), with the LT and HT peaks shifted to lower temperatures. The LT peak increased in intensity, while the HT peak ended at around 450 °C, instead of at the value of ca. 550 °C observed for the bare zeolite. This could be explained by coverage of the strongest acid sites by vanadium oxide species. The quantities of desorbed NH_3 were higher for all the samples containing vanadium oxide, reflecting a predominance of weak Lewis acid sites [50,51].

3.2. Characterization of the vanadium oxide-impregnated zeolites

Quantitative phase analyses of the diffraction patterns for the impregnated VA, VB, VC, and VD catalysts (Fig. S1) revealed small quantities of crystalline V_2O_5 species. In terms of zeolite crystallinity, the XRD patterns were similar to those for the bare zeolites. In the treatment of the XRD data, the crystallography information file (CIF) from the International Zeolite Association (IZA) was adopted for the MFI zeolite, while the 29140 standard from the ICSD database was used for V_2O_5. From comparison of the samples, a crystalline V_2O_5 mass fraction of 9.0% was obtained for the parent

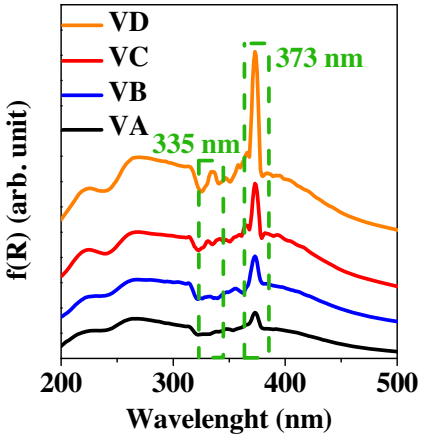

Fig. 5. UV–Vis diffuse reflectance spectra of samples containing vanadium oxide.

catalyst, which was very close to the 10% mass percentage used in preparation of the samples, while V_2O_5 mass fractions between 4% and 6.5% were obtained for the desilicated and acid treated samples. This effect of dispersion on the support, with production of poorly crystallized V_2O_5 particles, could be attributed to the creation of mesopores and the capacity to cover the zeolite surface during the wet impregnation process. Comparison of the mesopore volumes of the bare and impregnated zeolites (Table 1) confirmed the dispersion of V_2O_5 in the mesopores. The important influence of V_2O_5 dispersion on catalytic activity is discussed below.

The diffuse reflectance spectroscopy measurements in the UV–Vis region (Fig. 5) showed distinct results for the impregnated samples. The shapes of the spectra in this region were influenced by the local structures of the vanadium atoms. For example, the spectral range 333–500 nm provides information about the transfer of low energy electrons between O and V^{5+} for vanadium atoms in octahedral coordination [52,53]. On the other hand, the range 285–333 nm is related to vanadium in tetrahedral coordination. The green dashed rectangle highlighted in Fig. 5 indicates a region influenced by the vanadium oxide environment. Bands at 335 nm and 373 nm were due to electron charge transfer of V^{5+} with terminal or bridging oxygen anions, respectively. In other words, the highlighted region was associated with terminal and supported vanadium oxides. The main peak occurred at 384 nm, although shifts to higher energy (or lower wavelength) could occur, depending on the degree of vanadium oxide coordination by water. Hence, the systematic increase in intensity of this band complemented the previous finding of greater dispersion of V_2O_5 on the porous zeolites.

3.3. Catalytic activity

3.3.1. Step 1 – glycerol dehydration

The glycerol dehydration reaction occurs in two sequential reactions. In the first reaction step, glycerol dehydrates on acid sites, giving rise to a water molecule and a very reactive 3-hydroxypropene intermediate that rapidly isomerizes via a keto-enol rearrangement to 3-hydroxypropanal. The 3-hydroxypropanal molecule then dehydrates, releasing water and acrolein. This reaction sequence occurs at protonic Brønsted acid sites [12,30,54]. In contrast to the performance of the acid sites of the zeolites, a plot obtained using a reference alumina (which mainly contained Lewis acid sites) as catalyst reflected low levels of activity and stability in the reaction (Fig. 6, Table 2).

The catalytic results obtained for samples A, B, C, and D are summarized in Fig. 6. Regardless of the sample or the reaction time, the main product of glycerol dehydration was acrolein. Glycerol conversions of 88% and 87% were achieved using sample A and desilicated sample B, respectively. The beneficial effect of the micro-mesoporosity of sample B was shown by a decrease in catalyst deactivation from 19% to 7%.

The acid treated samples (C and D) both showed glycerol conversion exceeding 90% during the first hour of reaction. However, there was more pronounced deactivation of the sample treated with hydrochloric acid (sample D), with deactivation values of 5.2% and 18.4% for samples C and D, respectively. These findings indicated that both acids caused leaching of EFA (Table 1), and that HCl was less selective than oxalic acid, because it also removed part of the structural aluminum, damaging the zeolite structure and consequently affecting the activity of the catalyst in the reaction.

As mentioned before, all the samples were more selective to acrolein, compared to other reaction products such as acetaldehyde, 3-hydroxypropanal, and acetol (Fig. 7). The product distributions obtained for sample A after 1 and 6 h (Fig. S2) were indicative of decreased selectivity to acetaldehyde (2 carbon atoms) and increased selectivity to 3-hydroxypropanal (3 carbon atoms). This suggested that decomposition of the primary molecule occurred at the beginning of the reaction, and that this decomposition was associated with coke formation and CO_x release [30]. The decomposition was related to contact of the glycerol molecule and products with strong acid sites on the catalyst surface that became progressively covered with coke, resulting in deactivation of the strong acid sites. This was also reflected in the lower selectivity to

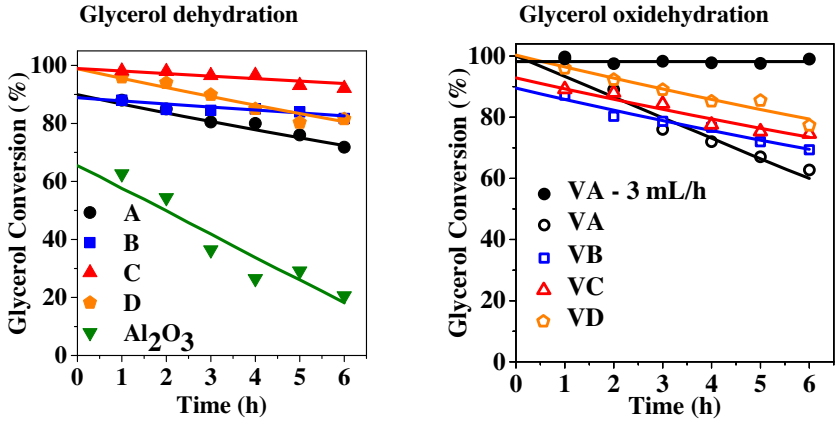

Fig. 6. Glycerol dehydration and oxidehydration of samples without (left plot) and with vanadium oxide (right plot). The filled and empty symbols correspond to flows of 3.0 mL/h and 6.0 mL/h of glycerol solution, respectively.

Table 2
Reactant flow, conversion at time zero, catalyst deactivation, and %wt. of coke after 6 h on glycerol stream: (1) glycerol dehydration, and (2) glycerol oxidehydration.

Reaction	Catalyst	10 wt.% glycerol solution flow (mL/h)	Conversion at time zero (%)	Catalyst deactivation (%)	% wt. of coke
(1)	A	3	90	19.4	12.6
	B		89	7.0	15.5
	C		100	5.2	17.8
	D		100	18.4	14.1
	Al_2O_3		65	68.5	55.5
(2)	V-A	6	100	42.4 (0.0)[a]	12.8 (4.7)
	V-B		89	22.4 (0.0)	12.2
	V-C		93	20.9 (0.0)	10.4
	V-D		100	20.9 (0.0)	14.4

[a] In brackets are indicated the results of catalyst deactivation under a flow of 3.0 mL/h of glycerol solution.

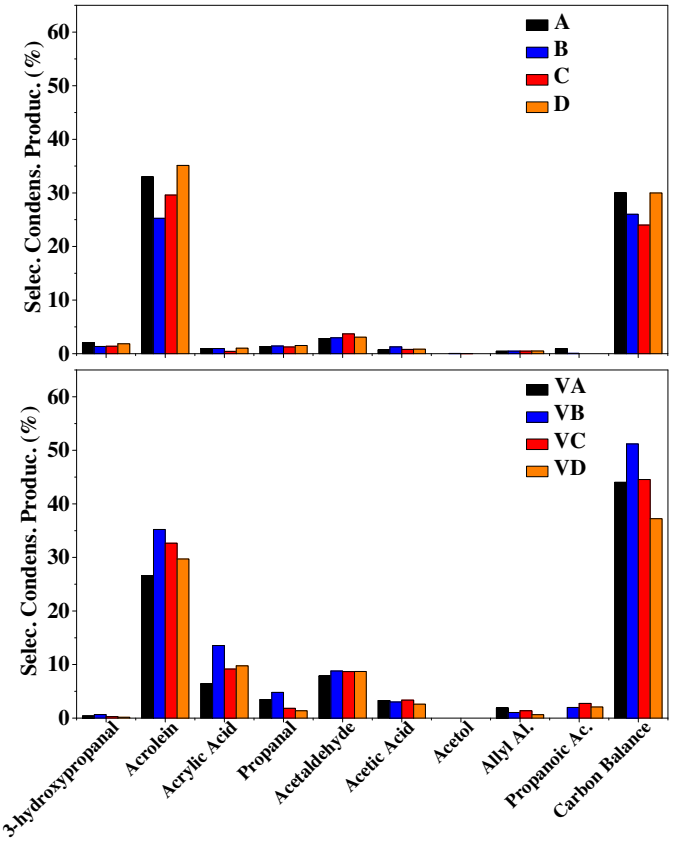

Fig. 7. Selectivity towards condensable products and carbon balance in dehydration (top) and oxidehydration (bottom) of the catalysts during 1 h of reaction at 300 °C and 350 °C, respectively.

acetic acid after 6 h of reaction (Fig. S2), since acetic acid is a product formed from acetaldehyde oxidation. Furthermore, and most importantly, there was increased selectivity to acrolein.

Different behavior was observed for samples B, C, and D, with greater amounts of carbonaceous deposits detected, compared to the parent zeolite, despite lower deactivation. The thermogravimetric analyses of the spent catalysts (Fig. S3) enabled establishment of relationships between the mesopore volumes and the amounts of carbonaceous compounds deposited on the catalysts, based on the weight loss. In the case of the purely microporous sample A, the coke was mainly deposited within straight and sinusoidal micropores, or in the entrances of pores, blocking the access of new glycerol molecules. The effect of coke on catalytic performance was more noticeable, even for low coke contents. In porous zeolites, the coke is preferentially located in the intra-crystalline pockets created by desilication with NaOH and acid leaching, maintaining the micropores available for glycerol [24].

3.3.2. Steps 1 and 2 – glycerol oxidehydration

As mentioned before, the two steps of glycerol oxidehydration are (i) the dehydration of glycerol to acrolein on acid sites [2,30], and (ii) the conversion of acrolein to acrylic acid on redox sites [55]. Therefore, in the impregnated catalysts, the catalytic sites responsible for glycerol dehydration were the Brønsted acid sites, while V_2O_5 (better represented as V_2O_{5-x}) was responsible for acrylic acid formation. The V_2O_5 impregnation affected the acid sites of the catalysts, increasing the contribution of the Lewis acid sites and covering the strong Brønsted acid sites, as observed from the TPD-NH_3 analyses. As reported previously, the amount of impregnated V_2O_5 significantly affected the proportions of acid and redox sites, leading to substantial alterations in catalyst activity [26]. The main difference between the two groups of samples concerned catalyst stability. No deactivation at all was observed for the samples impregnated with vanadium oxide. In order to be able to observe the deactivation and compare samples B, C, and D, the flow of glycerol fed to the reactor was increased from 3 to 6 mL/h (see VA results in Fig. 6, open and closed symbols). This change enabled detection of 42.4% deactivation of the VA catalyst. Despite the deactivation under this new experimental condition, the presence of vanadium oxide reduced the loss of catalytic activity, compared to the bare zeolites, demonstrating the multifunctional characteristics of these catalysts in promoting conversion, with selectivity to acrylic acid and stability of catalytic activity over longer periods.

The desilicated and impregnated sample (VB) showed decreased deactivation in the dehydration reaction, compared to the VA catalyst, similar to the behavior observed for the bare zeolites. The coke was deposited in the formed mesopores, avoiding obstruction of the micropores. In addition, the removal of EFA by the action of oxalic acid, followed by impregnation (catalyst VC), resulted in a further small reduction in deactivation, which decreased to 20.9%.

An interesting result was obtained for the sample treated with hydrochloric acid and impregnated with V_2O_5 (sample VD). This zeolite and the reference alumina showed the highest levels of deactivation in the dehydration of glycerol. However, in the oxidehydration reaction, the VD catalyst presented deactivation very close to that of the VC catalyst, because the action of vanadium oxide helped to reduce coke formation by oxidizing smaller coke molecules before oligomerization. Furthermore, the mesoporosity helped in dispersing vanadium oxide on the surface of the zeolite, as confirmed by the UV–vis analysis that showed an increase in the signal at 335–373 nm.

The distribution of the products was also affected by the treatments applied to the samples (Fig. 7 and S3). Use of sample VA resulted in 5% of acrylic acid after the first hour on stream, with selectivity to acrylic acid increasing to 25% after 6 h. These samples contained an average of 12 wt.% coke, so the shift in the acrylic

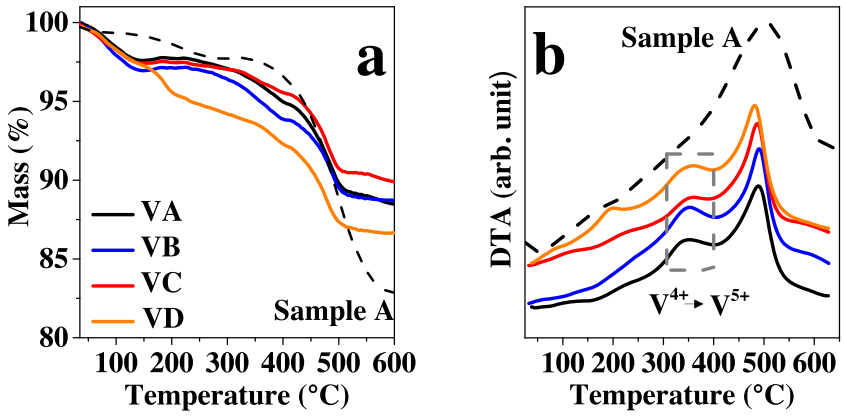

Fig. 8. TG (a) and DTA (b) curves of the catalysts impregnated with vanadium oxide after 6 h of reaction.

acid yield could be explained by the coverage by coke of the more deactivating sites. It should be noted that the acrylic acid selectivity showed a dependence on the glycerol flow. A flow of 3.0 mL/h was not only beneficial to catalyst stability, but also enabled selectivity to acrylic acid of 17% to be achieved in the first hour. Conditions providing greater selectivity could therefore be obtained by adjusting the glycerol contact time. The initial acrylic acid selectivity of the VB catalyst (14%) was higher than obtained for the VA sample.

Other products of glycerol oxidehydration are acetic acid and acetaldehyde, which both arise from the bifunctional nature of the catalyst. The acid sites crack the initial three carbon atoms of the glycerol molecule, resulting in acetaldehyde and one molecule of CO_x. The presence of O_2 then leads to the oxidation of acetaldehyde to acetic acid. The selectivities to these two products were lower than 10% in the first hour of reaction, and decreased after 6 h due to deactivation of the sites. This behavior was the opposite of that observed for the acrylic acid selectivity, suggesting that the same sites were involved. The carbon balance between the glycerol feed and the outflowing condensable liquid products increased with the glycerol flow and in the presence of V_2O_5. At glycerol solution flow rates of 3.0 mL/h (for the bare zeolites) and 6.0 mL/h (for the impregnated samples), the average carbon balances were 30% and 55%, respectively.

The activity results showed that the mesopores in the catalysts assisted the mass transport of reactant and products, and therefore promoted the catalytic activity. In addition, the formation of the extra porosity assisted in accommodation of the much less volatile polymeric coke molecules, which remained deposited in the intra-crystalline pockets within the zeolite mesopores, hence maintaining access to the micropores. Two types of coke are formed in glycerol reactions: (1) polyaromatic compounds formed in radical reactions, and (2) polyglycols formed by the condensation of neighboring glycerol molecules [26]. Previous characterization studies [20–22] have shown that both types are present in bare zeolites, while the polyglycol type is suppressed following impregnation with V_2O_5.

The results of the thermogravimetric analyses of the spent catalysts are shown in Fig. 8. The DTA curves of the catalysts with vanadium oxide showed two exothermic peaks (Fig. 8b). The first peak, at lower temperature (~350 °C), was associated with the re-oxidation (exothermic event) of vanadium species (V^{4+} to V^{5+}) in the case of the spent V_2O_5/ZSM-5 catalysts [20]. The second peak, at about 500 °C, was due to polyaromatics (known as stubborn coke) [8,56,57]. In the first temperature region, some samples showed a slight increase in mass (Fig. 8a), associated with the oxidation of V^{4+} to V^{5+} (highlighted in Fig. 8b) [26]. The VD sample showed a small peak near 200 °C, which could have been related to the decomposition of carbonaceous species on the catalyst surface. The high porosity of this sample (Table 1) was likely to have contributed to the oxidation of coke precursors at low temperatures. For comparison, the thermogram of the most coked sample A is present in Fig. 8a . The largest DTA signal (Fig. 8b) represents the two species of coke formed.

As mentioned, despite the Lewis acid sites are formed in large amounts after V_2O_5 impregnation, condition that could damage the catalytic activity as shown for γ-Al_2O_3, the maintenance of Brønsted acid sites with the coverage of the strong Brønsted acid sites by the impregnation was an important aspect for maintaining catalytic activity for a prolonged time.

4. Conclusions

The alkaline treatment of ZSM-5 zeolite with NaOH was effective for obtaining a micro-mesoporous zeolite by partial disruption of the crystalline framework due to silicon removal. A portion of the framework aluminum atoms in tetrahedral coordination was also removed, but due to their low solubility, these atoms remained on the zeolite as EFA (extra-framework aluminum). The removal of EFA was achieved by subsequent acid treatment using either hydrochloric acid or oxalic acid. The latter was more effective, because although hydrochloric acid acted to dissolve oligomeric aluminum oxide species, it also attacked the crystalline zeolite structure, while oxalic acid additionally acted as a chelating agent. The micro-mesoporous zeolites were subsequently impregnated with vanadyl sulfate solution and calcined to form supported V_2O_5. Spectroscopic measurements in the UV–Vis region indicated that V_2O_5 was well dispersed on the porous zeolites, due to the high pore volumes. The dispersion of V_2O_5 increased the quantity of acid sites on the zeolites. The beneficial effects of micro-mesoporosity and V_2O_5 dispersion could be seen in the performance of the catalysts during glycerol conversion. The selectivities to acrolein and acrylic acid were enhanced, and the smaller amounts of coke led to reduced deactivation.

Acknowledgements

This work was supported by the Brazilian agencies CNPq (grants 473456/2012-5 and 401679/2013-6) and FAPESP (grants 2013/10204-2, 2013/50023-7 and 2014/11952-5). The authors also thank the Brazilian Synchrotron Light Laboratory (LNLS) in Campinas for use of the XPD beamline (proposal XPD-17839).

Appendix A. Supplementary data

Supplementary data associated with this article can be found, in the online version, at http://dx.doi.org/10.1016/j.cattod.2016.08.005.

References

[1] B. Katryniok, S. Paul, V. Belliere-Baca, P. Rey, F. Dumeignil, Green Chem. 12 (2010) 2079–2098.
[2] B. Katryniok, S. Paul, F. Dumeignil, ACS Catal. 3 (2013) 1819–1834.
[3] C.A.G. Quispe, C.J.R. Coronado, J.A. Carvalho Jr., Renew. Sustainable Energy Rev. 27 (2013) 475–493.
[4] M.A. Dasari, P.P. Kiatsimkul, W.R. Sutterlin, G.J. Suppes, Appl.Catal. A-Gen. 281 (2005) 225–231.
[5] T. Miyazawa, Y. Kusunoki, K. Kunimori, K. Tomishige, J. Catal. 240 (2006) 213–221.
[6] J. Chaminand, L. Djakovitch, P. Gallezot, P. Marion, C. Pinel, C. Rosier, Green Chem. 6 (2004) 359–361.
[7] P.K. Vanama, A. Kumar, S.R. Ginjupalli, V.R.C. Komandur, Catal. Today 250 (2015) 226–238.
[8] H. Atia, U. Armbruster, A. Martin, J. Catal. 258 (2008) 71–82.
[9] F. Wang, J.-L. Dubois, W. Ueda, Appl. Catal. A-Gen. 376 (2010) 25–32.
[10] F. Cavani, S. Guidetti, L. Marinelli, M. Piccinini, E. Ghedini, M. Signoretto, Appl. Catal. B-Environ. 100 (2010) 197–204.
[11] N.R. Shiju, D.R. Brown, K. Wilson, G. Rothenberg, Top. Catal. 53 (2010) 1217–1223.
[12] J. Deleplanque, J.L. Dubois, J.F. Devaux, W. Ueda, Catal. Today 157 (2010) 351–358.
[13] Y.T. Kim, K.-D. Jung, E.D. Park, Appl. Catal. A-Gen. 393 (2011) 275–287.
[14] C.S. Carriço, F.T. Cruz, M.B. Santos, D.S. Oliveira, H.O. Pastore, H.M.C. Andrade, A.J.S. Mascarenhas, J. Catal. 334 (2016) 34–41.
[15] W.Y. Pan, L. Huang, F. Qin, Y. Zhuang, X.M. Li, J.X. Ma, W. Shen, H.L. Xu, Acta Phys. Chim. Sin. 31 (2015) 965–972.
[16] J.P. Lourenco, M.I. Macedo, A. Fernandes, Catal. Commun. 19 (2012) 105–109.
[17] J.A. Cecilia, C. Garcia-Sancho, J.M. Merida-Robles, J.S. González, R. Moreno-Tost, P. Maireles-Torres, Appl. Catal. A-Gen. 516 (2016) 30–40.
[18] A.S. Paula, L.G. Possato, D.R. Ratero, J. Contro, K. Keinan-Adamsky, R.R. Soares, G. Goobes, L. Martins, J.G. Nery, Microporous Mesoporous Mater. 232 (2016) 151–160.
[19] L. Shen, H. Yin, A. Wang, Y. Feng, Y. Shen, Z. Wu, T. Jiang, Chem. Eng. J. 180 (2012) 277–283.
[20] L. Shen, H. Yin, A. Wang, X. Lu, C. Zhang, F. Chen, Y. Wang, H. Chen, J. Ind. Eng. Chem. 20 (2014) 759–766.
[21] M. Dolores Soriano, P. Concepcion, J.M. Lopez Nieto, F. Cavani, S. Guidetti, C. Trevisanut, Green Chem. 13 (2011) 2954–2962.
[22] A. Chieregato, F. Basile, P. Concepcion, S. Guidetti, G. Liosi, M. Dolores Soriano, C. Trevisanut, F. Cavani, J.M. Lopez Nietoc, Catal. Today 197 (2012) 58–65.
[23] A. Chieregato, M. Dolores Soriano, F. Basile, G. Liosi, S. Zamora, P. Concepcion, F. Cavani, J.M. Lopez Nieto, Appl. Catal. B-Environ. 150 (2014) 37–46.
[24] L. Shen, H. Yin, A. Wang, X. Lu, C. Zhang, Chem. Eng. J. 244 (2014) 168–177.
[25] A. Chieregato, M.D. Soriano, E. Garcia-Gonzalez, G. Puglia, F. Basile, P. Concepcion, C. Bandinelli, J.M.L. Nieto, F. Cavani, ChemSusChem 8 (2015) 398–406.
[26] L.G. Possato, W.H. Cassinelli, T. Garetto, S.H. Pulcinelli, C.V. Santilli, L. Martins, Appl. Catal. A: Gen. 492 (2015) 243–251.
[27] L.H. Vieira, K.T. Carvalho, E.A. Urquieta-González, S.H. Pulcinelli, C.V. Santilli, L. Martins, J. Mol. Catal. A: Chem. (2015), http://dx.doi.org/10.1016/j.molcata.2015.12.019 (in press).
[28] M.V. Rodrigues, C. Vignatti, T. Garetto, S.H. Pulcinelli, C.V. Santilli, L. Martins, Appl. Catal. A: Gen. 495 (2015) 84–91.
[29] H. Decolatti, B. Dalla Costa, C. Querini, Microporous Mesoporous Mat. 204 (2015) 180–189.
[30] L.G. Possato, R.N. Diniz, T. Garetto, S.H. Pulcinelli, C.V. Santilli, L. Martins, J. Catal. 300 (2013) 102–112.
[31] J.C. Groen, J.C. Jansen, J.A. Moulijn, J. Perez-Ramirez, J. Phys. Chem. B 108 (2004) 13062–13065.
[32] J.C. Groen, L.A.A. Peffer, J.A. Moulijn, J. Perez-Ramirez, Microporous Mesoporous Mat. 69 (2004) 29–34.
[33] J.C. Groen, T. Bach, U. Ziese, A. Donk, K.P. de Jong, J.A. Moulijn, J. Perez-Ramirez, J. Am. Chem. Soc. 127 (2005) 10792–10793.
[34] J.C. Groen, L.A.A. Peffer, J.A. Moulijn, J. Perez-Ramirez, Chem. A Eur. J. 11 (2005) 4983–4994.
[35] J.C. Groen, J.A. Moulijn, J. Perez-Ramirez, J. Mater. Chem. 16 (2006) 2121–2131.
[36] J.C. Groen, W. Zhu, S. Brouwer, S.J. Huynink, F. Kapteijn, J.A. Moulijn, J. Perez-Ramirez, J. Am. Chem. Soc. 129 (2007) 355–360.
[37] J. Perez-Ramirez, C.H. Christensen, K. Egeblad, C.H. Christensen, J.C. Groen, Chem. Soc. Rev. 37 (2008) 2530–2542.
[38] P. Mars, D.W. Van Krevelen, Chem. Eng. Sci. 3 (1954) 41–59.
[39] D. Verboekend, S. Mitchell, M. Milina, J.C. Groen, J. Perez-Ramirez, J. Phys. Chem. C 115 (2011) 14193–14203.
[40] H. Canova, A. Fontoura, R. Neuenschwander, B. Diaz, C. Rodella, Upgrades to the XRD1 beamline optics and endstation at the LNLS, J. Phys. Conf. Series IOP Publ. (2014) (p. 012004).
[41] B. Toby, J. Appl. Crystallogr. 34 (2001) 210–213.
[42] A.F. Gualtieri, S. Ferrari, M. Leoni, G. Grathoff, R. Hugo, M. Shatnawi, G. Paglia, S. Billinge, J. Appl. Crystallogr. 41 (2008) 402–415.
[43] V. Paixao, R. Monteiro, M. Andrade, A. Fernandes, J. Rocha, A.P. Carvalho, A. Martins, Appl. Catal. A-Gen. 402 (2011) 59–68.
[44] R. Giudici, H.W. Kouwenhoven, R. Prins, Appl. Catal. A-Gen. 203 (2000) 101–110.
[45] J.T. Smith, S. Bailey, Acta Crystallogr. 16 (1963) 801–811.
[46] Z.M. Yan, M.A. Ding, J.Q. Zhuang, X.C. Liu, X.M. Liu, X.W. Han, X.H. Bao, F.X. Chang, L. Xu, Z.M. Liu, J. Mol. Catal. A-Chem. 194 (2003) 153–167.
[47] M.R. Apelian, A.S. Fung, G.J. Kennedy, T.F. Degnan, J. Phys. Chem. 100 (1996) 16577–16583.
[48] S. Storck, H. Bretinger, W.F. Maier, Appl. Catal. A-Gen. 174 (1998) 137–146.
[49] A.W. Chester, E.G. Derouane, Zeolite Charact. Catal. A Tutorial (2009).
[50] M. Petras, B. Wichterlova, J. Phys. Chem. 96 (1992) 1805–1809.
[51] S.S.R. Putluru, A. Riisager, R. Fehrmann, Appl. Catal. B-Environ. 97 (2010) 333–339.
[52] X.T. Gao, I.E. Wachs, J. Phys. Chem. B 104 (2000) 1261–1268.
[53] L.J. Burcham, G. Deo, X.T. Gao, I.E. Wachs, Top. Catal. 11 (2000) 85–100.
[54] B. Katryniok, S. Paul, M. Capron, C. Lancelot, V. Belliere-Baca, P. Rey, F. Dumeignil, Green Chem. 12 (2010) 1922–1925.
[55] D. Vitry, Y. Morikawa, J.L. Dubois, W. Ueda, Appl. Catal. A-Gen. 251 (2003) 411–424.
[56] C.-J. Jia, Y. Liu, W. Schmidt, A.-H. Lu, F. Schueth, J. Catal. 269 (2010) 71–79.
[57] Y.T. Kim, K.-D. Jung, E.D. Park, Appl. Catal. B-Environ. 107 (2011) 177–187.